Acta Geotechnica (2021) 16:1949–1960
https://doi.org/10.1007/s11440-021-01140-w

SHORT COMMUNICATION

Construction of soil–water characteristic curve of granular materials with toroidal model and artificially generated packings

Bate Bate[1] · Shaokai Nie[1] · Zejian Chen[2] · Fengshou Zhang[3] · Yunmin Chen[1]

Received: 28 April 2020 / Accepted: 6 January 2021 / Published online: 25 January 2021

Abstract

The soil–water characteristic curve (SWCC) of granular materials is crucial for many emerging engineering applications, such as permeable pavement and methane hydrate extraction. Laboratory determination of the SWCC of granular materials suffers from inaccurate volume readings by the diffused air bubbles in the hanging column and sudden desaturation at small matric suction intervals. Theoretical determination of the SWCC of granular materials also suffers from semi-empirical nature in the prediction from grain size distribution, or from the limitation of assumed cubic packing or face-centred cubic packing with a toroid meniscus water model. In this study, real three-dimensional particle packing was first rendered with the discrete element method using approximation of spheres. Then, the Young–Laplace equation was applied to calculate the volume of toroidal meniscus water between each pair of spheres, which adds to the water content in the pendular regime of the SWCC. Additionally, a digitized image algorithm was used to identify the pore throats and calculate the air entry value and residual matric suction, the connection of which yields a straight line approximating the funicular regime. The SWCC was thus constructed. Comparison with laboratory-measured SWCCs suggested that although reasonable agreement was reached in general for glass beads, residual water content was underestimated, especially for non-spherical granular materials. Several possible reasons were discussed including the existence of patchy water accounting for the major portion of water in the beginning of pendular regime of granular materials, which was also observed in microscopic photographs through a special desaturation experiment.

Keywords Soil–water characteristic curve · Granular materials · Packing · Toroidal model · Discrete element method

1 Introduction

The soil–water characteristic curve (SWCC) of granular materials is a crucial property for many emerging engineering applications, such as permeable pavement, geotechnical structures made of construction and demolished wastes, ocean methane hydrate extraction, and CO_2 imbibition in enhanced oil recovery. Comprising a relationship between matric suction and water content, SWCC characterizes the key properties of unsaturated soil and can be used to derive many mechanical properties including shear strength, stiffness, consolidation and hydraulic conductivity [5, 8, 23, 24, 26, 33, 40]. Matric suction Ψ, originating from meniscus water [6] is the difference of air pressure and pore water pressure (i.e. $u_a - u_w$). Laboratory determination of SWCC of granular materials often involves a hanging column. The accuracy of the measured SWCC suffers from diffused air bubbles in the volume reading in the hanging column and sudden desaturation at small matric suction values. Semi-empirical formulas were also used in predicting the SWCC from grain size distribution (e.g. [7, 35], while the physical meanings of the associated fitting parameters are mostly unclear.

There are four regimes in the SWCC, namely (1) saturated regime (saturated with non-negative pore water pressure); (2) capillary regime (saturated with negative

✉ Zejian Chen
ze-jian.chen@connect.polyu.hk

[1] Institute of Geotechnical Engineering, College of Civil Engineering and Architecture, MOE Key Laboratory of Soft Soils and Geoenvironmental Engineering, Zhejiang University, Hangzhou, China

[2] Department of Civil and Environmental Engineering, The Hong Kong Polytechnic University, Hong Kong SAR, China

[3] Department of Geotechnical Engineering, College of Civil Engineering, Tongji University, Shanghai, China

pore water pressure); (3) funicular regime (continuous water and air phases with matric suction > air entry value (AEV)); and (4) pendular regime (discontinuous water phase and continuous air phase) [5, 6, 30]. In pendular regime, water was perceived to be mainly in the form of liquid bridges (meniscus toroid) and absorbed films [18, 28]. The volume of meniscus toroid between a pair of ideal spherical particles of different sizes under a given matric suction can be described by the Young–Laplace equation [4, 17, 19, 32]. By combining the solution with a certain particle packing, the macroscopic SWCC of granular materials can be predicted. Two basic types of ideal particle packings, namely simple cubic packing and face-centered packing, are often built to simulate the loosest and densest situation, respectively [2, 3, 13, 21]. However, they fail to represent an actual packing state. Therefore, actual particle size distribution and porosity were also taken into consideration in recent mathematical simulations by establishing the distribution of pore sizes [20, 34, 36]. Gan et al. [9] adopted a complicated particle–water discrete element method to investigate the hysteresis of SWCC with considerations of real particle size distribution and random packing and achieved some reasonable results. To date, successful and simple construction of SWCC of granular particles by directly generating a real particle arrangement (e.g. by discrete element method) with definite theoretical basis is still very limited.

The objective of this study is to propose a new method to predict the SWCC of granular materials. The following tasks were carried out: (1) generating a 3D rendition of spherical particles at realistic porosity to simulate granular materials with discrete element method; (2) employing the Young–Laplace equation to calculate the volume of toroidal meniscus water between each pair of spheres, which adds to the water content in the pendular regime of SWCC; (3) using a digitized image algorithm to simulate the connectivity of pores and calculate the air entry value and the residual matric suction, which define the beginning and the end of the funicular regime. Through the above steps, SWCC was constructed. Finally, the performance of the proposed SWCC model was evaluated with comparisons of measured data and microscopic photographs.

2 Theoretical models for the construction of SWCC in microscopic scale

2.1 A numerical solution to the Young–Laplace equation for the toroidal meniscus model in the pendular regime

Although granular materials are usually irregularly shaped, idealized spheres are used to simulate the particles in this study, which would greatly simplify the calculations. The toroidal meniscus model (also known as liquid bridge) (Fig. 1a) is often used to delineate the water phase between adjacent particles in the pendular regime, usually with the following assumptions: gravity is neglected, particles are spheres, and water only resides in the meniscus toroid near the contact between each pair of spheres. The geometrical configuration of the meniscus toroid depends on surface tension (T_s) and matric suction $\Psi = (u_a - u_w)$, as shown in Fig. 1b, which is described by the Young–Laplace equation:

$$(u_a - u_w) = T_s \cdot \left(\frac{1}{\rho_1} + \frac{1}{\rho_2}\right) \tag{1}$$

where ρ_1 and ρ_2 are the local curvature of the meniscus in orthogonal directions (Fig. 1b). The Young–Laplace equation is a second-order differential equation and its boundary conditions depend on liquid–solid contact angle, sphere radii and the gap between spheres. Many of the previous studies used circle approximation to solve the Young–Laplace equation, in which the curvature radius ρ_1 is considered constant. This approximation leads to a constant value of ρ_2, which disagrees with the reality and results in errors, especially for spheres with different sizes, as pointed out by some researchers [17, 24].

Consequently, it is important to adopt the exact solution of the Young–Laplace equation in calculating the configuration of the meniscus toroid. As the meniscus is a rotational surface, Eq. (1) can be transformed into Eq. (2), under a coordination system established in Fig. 1c:

$$\frac{\Psi}{T_s} = 2H = \frac{1}{\rho_1} + \frac{1}{\rho_2} = \frac{\ddot{r}}{(\dot{r}^2+1)^{3/2}} - \frac{1}{r(\dot{r}^2+1)^{1/2}} \tag{2}$$

where H represents the mean curvature of the meniscus. The boundary conditions can be written as follows:

$$\begin{cases} r|_{z=z_1} = R_1 \sin\alpha_1 & \text{(a)} \\ \dot{r}|_{z=z_1} = -\dfrac{1}{\tan(\alpha_1+\beta)} & \text{(b)} \\ r|_{z=z_2} = R_2 \sin\alpha_2 & \text{(c)} \\ \dot{r}|_{z=z_2} = \dfrac{1}{\tan(\alpha_2+\beta)} & \text{(d)} \end{cases} \tag{3}$$

Given matric suction Ψ, surface tension T_s, filling angles α_1, α_2, and contact angle β, the generatrix between two particles can be solved. However, as the filling angles are unknown, the analytical solutions are highly complicated and inconvenient to use [32]. To address this problem, Lian et al. [19] proposed a numerical solution for particle pairs with equal sizes based on the Euler method, which is extended in this study to consider arbitrary radii and inter-particle distance.

In Fig. 1(c), (X_i, Y_i) describe a series of dense points on the meniscus toroid generatrix. The values of Y_{i+1} at the

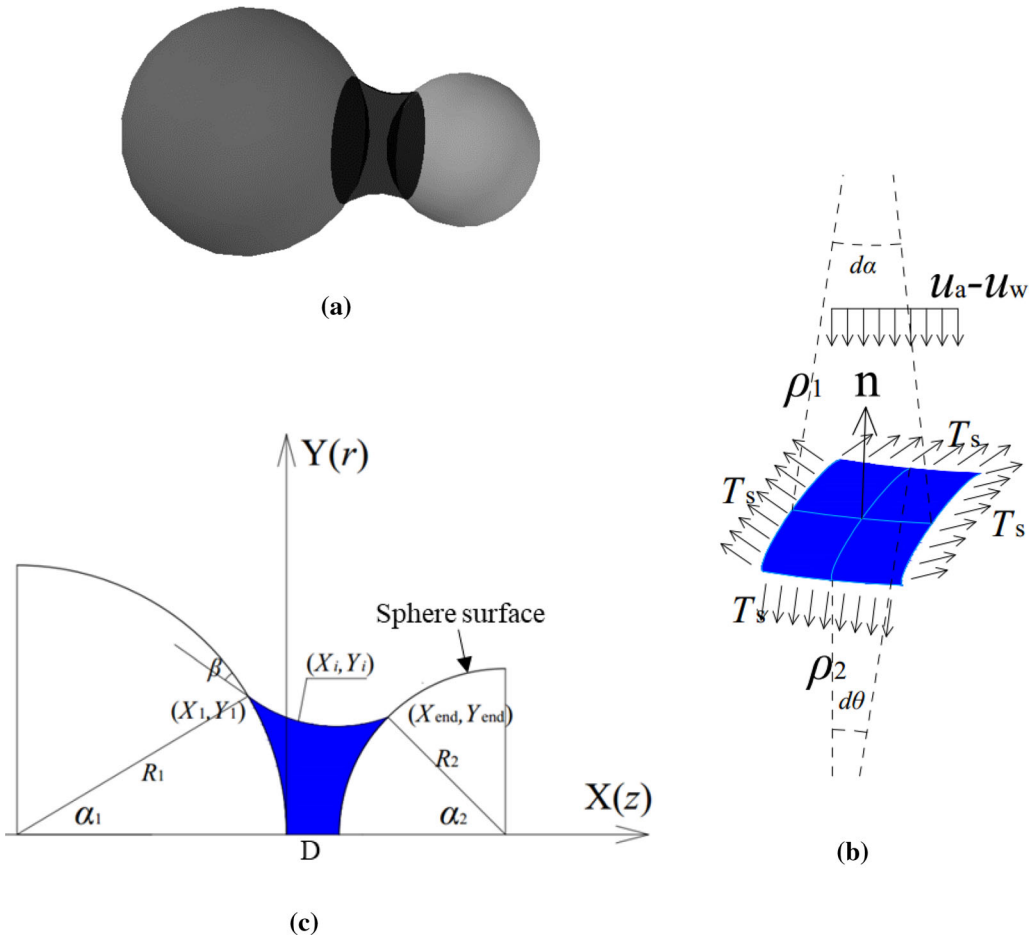

Fig. 1 Schematic diagrams of the meniscus toroid model: (**a**) A 3D diagram; (**b**) diagram of force balance of an area element on the meniscus; (**c**) A plane coordinate system for the numerical solution

point next to (X_i, Y_i) can be approximated by a second-order Taylor series:

$$Y_{i+1} = Y_i + \Delta X \cdot \dot{Y}_i + \frac{1}{2}\Delta X^2 \cdot \ddot{Y}_i \tag{4}$$

where $\dot{Y} = \frac{dY}{dX}$ and $\ddot{Y} = \frac{d^2Y}{dX^2}$. Meanwhile, by making the substitution $Q = 1 + \dot{Y}^2$ [19], Eq. (2) can be simplified as Eq. (5):

$$\frac{dQ}{dY} - \frac{2Q}{Y} = 4HQ^{3/2} \tag{5}$$

where $\frac{dQ}{dY} = \frac{dQ}{dX}\frac{dX}{dY} = 2\dot{Y}\ddot{Y}\frac{1}{\dot{Y}} = 2\ddot{Y}$. The solution of Eq. (5) is $\frac{Y}{Q^{1/2}} + HY^2 = C$, which can be written as Eq. (6):

$$\dot{Y}_i = \pm\left[\frac{Y_i^2}{(C - HY_i^2)^2} - 1\right]^{1/2} \tag{6}$$

By rewriting Eq. (5), we have:

$$\dot{Y}_i = \frac{1 + \dot{Y}_i^2}{Y_i} + 2H\left(1 + \dot{Y}_i^2\right)^{3/2} \tag{7}$$

With Eqs. (4), (6) and (7) and boundary conditions (3), the configuration of the generatrix can be solved point by point. As long as the interval ΔX is sufficiently small, the accuracy of the solution will be ensured.

As shown in Fig. 1c, the starting point (X_1, Y_1) on the generatrix curve is unknown, depending on the value of filling angle α_1. Therefore, an iteration algorithm based on MATLAB was developed. This algorithm mainly includes four steps: (1) Set the filling angle at the bigger sphere as $\alpha_1 = \frac{\frac{\pi}{2}-\beta}{1000} \cdot k$ (k varies from 1 to 1000) and obtain X_1, Y_1, $\dot{Y}_1$,$\ddot{Y}_1$ and C based on geometric relationships and Eqs. (6 and 7); (2) use Eq. (4) to extend the generatrix point by point, until it reaches the other sphere; (3) by looping k from 1 to 1000, different generatrix curves from different values of α_1 can be obtained; (4) among these generatrix curves, the only one that best-fits all the boundary conditions will be selected as the true generatrix for the meniscus toroid between the two spheres.

With this algorithm, generatrix curve can be obtained with the given Ψ, T_s, β, R_1, R_2 and inter-particle gap D. It is worth noting that for non-contacting pairs of particles,

there are two solutions under the same condition (Fig. 2). The generatrix curve with higher volume (i.e. higher α_1) was chosen as the exact solution to the Young–Laplace equation based on the minimum energy principle [12, 19].

After determination of the generatrix curve, toroid volume can be calculated accordingly. First, the total volume surrounded by meniscus can be expressed as Eq. (8):

$$V = \sum \pi Y_i^2 \Delta X \tag{8}$$

Within the total volume, the solid part is calculated by the integral:

$$V_{\text{cap1}} = \frac{2\pi}{3} R_1^3 \left[1 - (\cos\alpha_1)^3\right] - \pi R_1^3 \cos\alpha_1 \sin\alpha_1 \tag{9}$$

$$V_{\text{cap2}} = \frac{2\pi}{3} R_2^3 \left[1 - (\cos\alpha_2)^3\right] - \pi R_2^3 \cos\alpha_2 \sin\alpha_2 \tag{10}$$

And the meniscus toroid volume is:

$$V_w = V - V_{cap1} - V_{cap2} \tag{11}$$

The results calculated by this method were almost identical to the data given in [17] (Fig. 3), which were also verified by the tables provided by Orr et al. [32].

2.2 Influencing factors of the toroidal meniscus

The influences of particle size, matric suction, contact angle, and inter-particle gap on water content of an unsaturated system were investigated using the above-mentioned method, as shown in Figs. 4, 5 and 6.

Figure 4 shows different water-matric suction curves of three pairs of particles with different particle sizes. It is indicated that particle pairs with larger or unequal sizes tend to have lower values of V_w/V_{sphere}. This suggests that coarser and better-graded granular materials will have lower water content with the same matric suction.

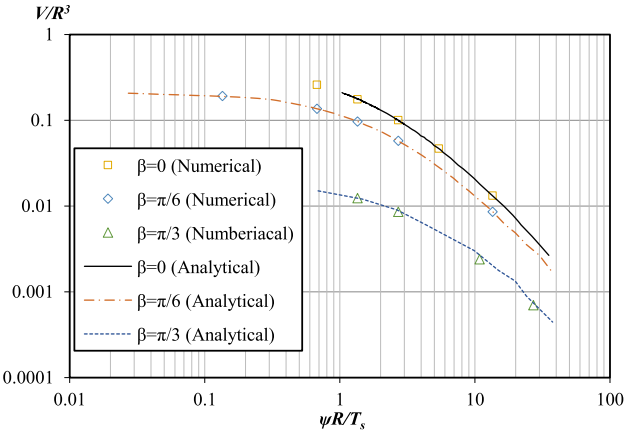

Fig. 3 Verification of the numerical solution in this study using the analytical solution in Lechman and Lu [17], in which β is the contact angle, R is the radius of the spheres and V is the volume of the water

Figure 5 shows that for a pair of spheres with 0.1 mm diameter, the shape of SWCC is dependent on the values of inter-particle gap D. On general, particles with larger D will have lower water content under the same matric suction. However, when D is very close to zero, the increase of D will cause the SWCC to move up slightly at the lower suction stage. Computation results also show that when D is larger than 0.02 mm, no water bridge can be formed between the two particles, indicating the existence of a limit of D for the formation of meniscus toroid.

Figure 6 shows that increasing contact angle results in lower water volume at the level of matric suction. This effect is one of the possible explanations to the hysteresis phenomenon of SWCCs during drying and wetting processes in the pendular regime, as the contact angle might be different in the two processes [9, 21].

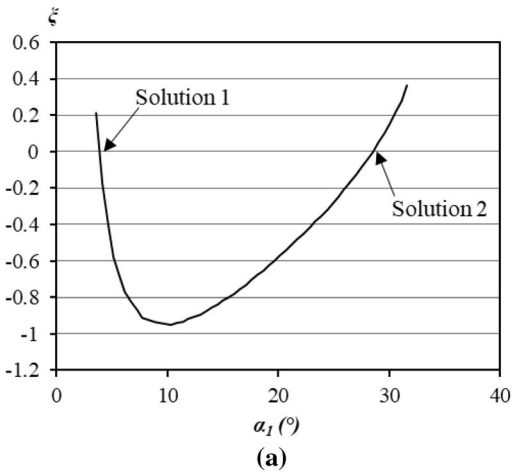

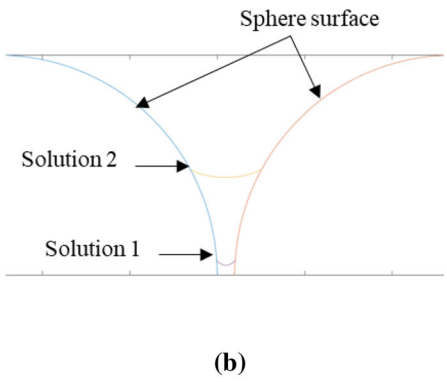

Fig. 2 Typical results of the algorithm. **a** The value of ξ approaches zero twice as α_1 increases; **b** the positions of two different generatrix solutions plotted in MATLAB as a result of **a**. ($\boldsymbol{\xi} = \left|\dot{\boldsymbol{Y}}_{\text{end}} - \tan\left(\frac{\pi}{2} - \boldsymbol{\beta} - \boldsymbol{\alpha}_2\right)\right|$ is an index in the algorithm to evaluate the convergence of the solution. The lower ξ is, the better a solution fits the boundary conditions)

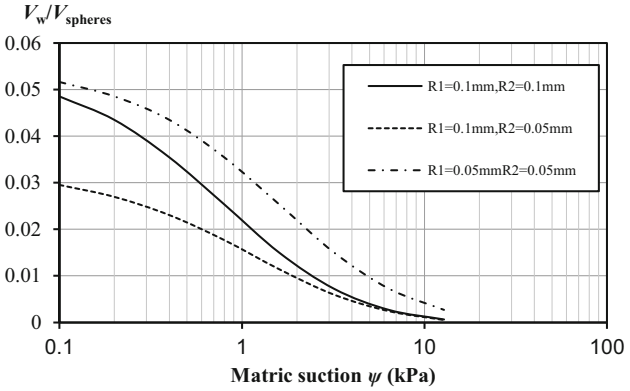

Fig. 4 Influence of particle size on the water retention curves of a pair of spheres (surface tension T_s = 0.0731 N/m, contact angle $\beta = 0°$, inter-particle gap $D = R_1/2$)

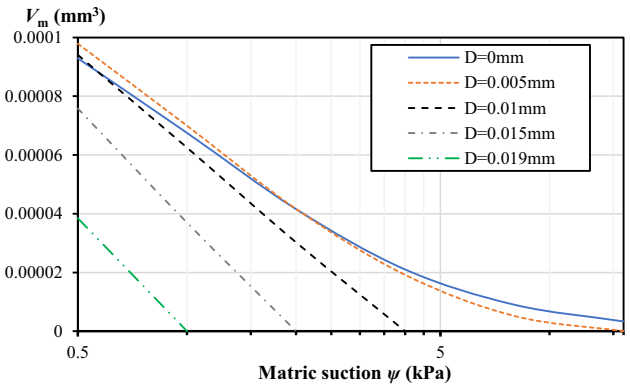

Fig. 5 Influence of inter-particle gap on the water retention curves of a pair of spheres (T_s = 0.0731 N/m, $R_1 = R_2$ = 0.1 mm, $\beta = 38.1°$)

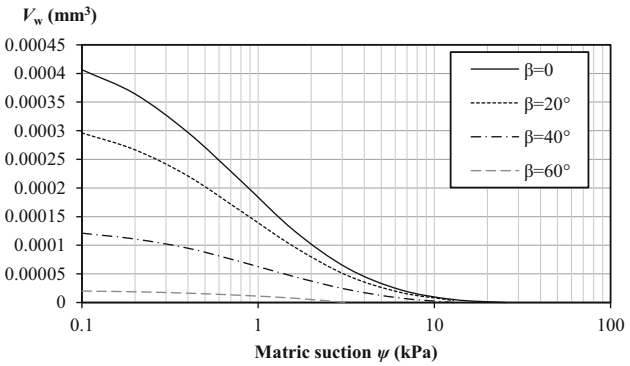

Fig. 6 Influence of contact angle on the water retention curves of a pair of spheres (T_s = 0.0731 N/m, $R_1 = R_2$ = 0.1 mm, D = 0.005 mm)

2.3 The microscopic model for the funicular regime

The toroidal meniscus model is only applicable for the pendular regime after the residual water content. At the funicular stage, many pores in the granular material are still filled with water. The water can flow in the channels formed by a series of pores, which are usually termed pore throats. A pore throat will transform from saturated to unsaturated state when its pore water shrinks into rings or films after the matric suction increases to a certain value (i.e. snap-off effect) [20]. The snap-off suction for an idealistic cylindrical throat can be calculated by Eq. 12 based on the Young–Laplace equation:

$$\psi_s = \frac{2T_s \cos\beta}{r} \tag{12}$$

where ψ_s is the snap-off suction and r is the radius of the throat. In granular materials, the size of pore throats is not uniform, which causes different values of ψ_s. In this study, the minimum ψ_s is used as the lower bound of suction (i.e. air entry value, AEV) in funicular regime, as the water begins to flow out from the largest pore throat. Meanwhile, the maximum ψ_s defines the upper bound of suction (i.e. residual suction) in funicular regime, as all pore throats will be unsaturated under this suction value. A straight line was drawn between AEV and residual suction to simulate the funicular regime.

In random packing models, it is hard, if possible, to simulate the equivalent radius r and calculate snap-off suction of each three-dimensional pore throat. A simplified process was therefore adopted to determine the snap-off suction of the pore throats within a porous model consisting of randomly packed particles, the details of which will be presented in the subsequent section.

3 Simulations of SWCC based on real particle packing

3.1 3D rendition of particle packing with the discrete element method

Packings of several granular material samples reported in the literature [2, 15, 27], were reconstructed with Particle Flow Code (PFC) ^{3D} 5.0 [14]. The original porosity (n), D_{50} and grain size distribution are shown in Table 1 and Fig. 7.

In the PFC model, granular particles are approximated to be spheres with different radii and distributed randomly in a box under the effect of gravity. Moreover, the Hertz contact model with the approximation theory of Mindlin and Deresiewicz [29] was employed in this study. Shear modular G and Poisson's ratio v are the two most important parameters, which were set as 30 GPa and 0.2, respectively. It was found after the trial-and-error process that with friction coefficient $\mu = 0.1$, particle overlap can be effectively reduced for glass beads. However, for Ottawa sands with higher porosity, 0.1 was too small to build the

models, and therefore, 0.5 was used for Ottawa sands. The built PFC model for each type of granular material contained around 4000 to 10,000 spheres, which is distributed in four cubic boxes. It should be noted that the numerical model represents a small soil element instead of the whole soil mass. The parameters of the DEM models are listed in Table 2, and a sample of simulated granular material is shown in Fig. 8. The particle distribution curves of models in PFC are very close to the input ones, as shown in Fig. 7.

3.2 Construction of SWCC in the pendular regime

The above sections yielded: (1) a meniscus toroid model with accurate numerical solution, which provides a relationship between the meniscus water volume and matric suction at the contact of two spherical particles; and (2) the real packing model of a macroscopic sample consisting of graded spheres, which was rendered with discrete element method at a measured porosity. Combining the above two results, the total meniscus water volume of this sample at a given matric suction, which was assumed to be homogeneous within the element [12], can be calculated by summing up the volumes of meniscus water between each possible pair of adjacent particles. Thus, the SWCC in the pendular regime can be obtained.

Water content can be converted to degree of saturation (S) by Eq. 13:

$$S = V_{\text{water}} / \left(V_{\text{solid}} \cdot \frac{n}{(1-n)} \right) \tag{13}$$

3.3 Construction of SWCC in the funicular regime

A digitized image algorithm was developed on MATLAB to determine the shapes of connected pore throats and to calculate snap-off matric suctions, as elaborated as follows. Firstly, slice the model parallelly into a number of layers along the vertical direction and obtain a binary image for

Table 1 Measured parameters of granular materials

Materials	Porosity n	D_{50} (mm)	Sources
Ottawa 20–30 sand	0.417	0.70	Cao et al. [2]
Ottawa 50–70 sand	0.447	0.23	Cao et al. [2]
0.25–0.60 mm glass beads	0.286	0.60	Manahiloh and Meehan 27
0.25–0.30 mm glass beads	0.375	0.25	Jaafar and Likos [15]

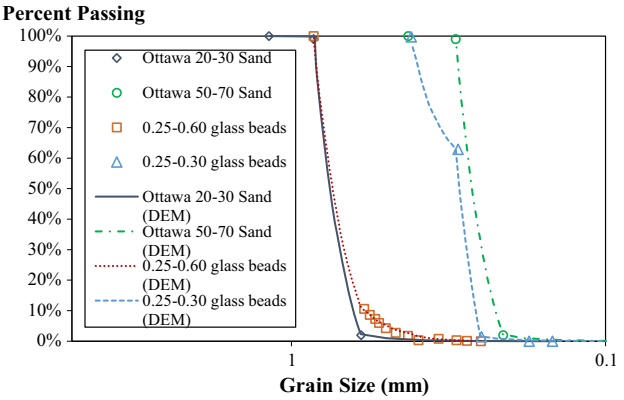

Fig. 7 Grain size distribution of four granular material samples used in the experiments and the simulated results by DEM

Table 2 Parameters of samples in DEM models

Materials	Porosity n	Coordination number	Friction coefficient μ	Other parameters
Ottawa 20–30 sand	0.417	4.68	0.5	G = 30 GPa
Ottawa 50–70 sand	0.447	5.08		
0.25–0.60 glass beads	0.286	6.55	0.1	υ = 0.2
0.25–0.30 glass beads	0.375	5.61		ρ = 2600 kg/m^3

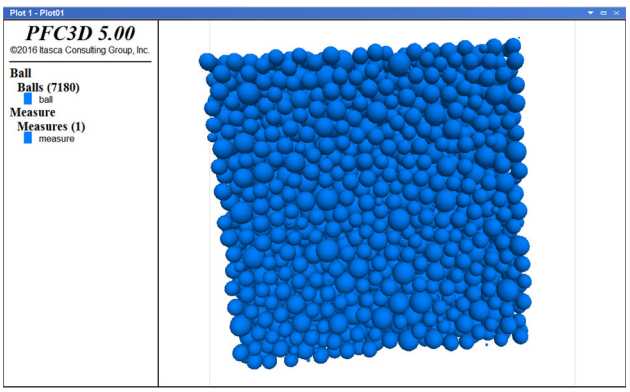

Fig. 8 The numerical model of a typical granular material built in PFC^{3D}

each layer, as shown in Fig. 9. Secondly, identify all independent two-dimensional pores for each layer after smoothing and filtering the images. The snap-off matric suction for each two-dimensional pore is calculated by:

$$\psi_s^{i,k} = \frac{T_s C \cos\beta}{A}, \quad k, i = 1, 2, \ldots \tag{14}$$

in which A represents the area of the pore, C is the perimeter, i is the pore ID, and k is the layer ID.

Thirdly, assuming that the drainage direction is from the bottom to the top boundary, all 2D pores at different layers can be connected from the bottom to the top via the overlaps and categorized into a certain number of connected pore throat "trees" in the three-dimensional space. For each connected 3D pore throat, the snap-off matric suction (ψ_s^i) is controlled by its maximum value within the whole pore throat ($\psi_s^i = \max\{\psi_s^{i,k}\}, k = 1, 2, \ldots$). The lower bound of ψ_s^i is the air entry value (AEV) [Eq. (15)], at which the sample begins to desaturate. The upper bound of ψ_s^i corresponds to residual suction (ψ_r) [Eq. (16)] at residual water content, which is the boundary between the funicular and pendular regime, where theoretically there are no saturated pores.

$$AEV = \min\{\psi_s^i\}, \quad i = 1, 2, \ldots \tag{15}$$

$$\psi_r = \max\{\psi_s^i\}, \quad i = 1, 2, \ldots \tag{16}$$

The degree of saturation at AEV is 100%, and the residual saturation degree is calculated by the Young–Laplace equation used in the pendular regime. Finally, the SWCC between the two limits is drawn as a straight-line segment to represent the funicular regime, which is a close approximation for coarse-granular materials as the major desaturation process does occur within a very small matric suction range. Thus, the SWCC involving the capillary, funicular, and pendular regimes has been constructed for a granular material sample.

3.4 Results

Calculated soil–water characteristic curves (SWCCs) with the above methods for four granular materials in drying process are shown in Fig. 10. Three features can be identified: (1) Predicted air entry values and residual matric suctions for the four materials were close to measured results; (2) predicted SWCCs in the funicular regime, i.e. a straight-line segment, were similar to the measured curves, which were also close to linear. The exception is that the measured residual degree of saturation of Ottawa 20–30 and 50–70 sands tends to be higher than the predicted values; (3) in the pendular regime, the simulated SWCCs of glass beads agree well with the measured ones, except for very few points where the simulated values were slightly lower. The predicted degree of saturation for both Ottawa 20–30 and 50–70 sands, however, is only a fraction of the measured ones. This phenomenon in the pendular regime is similar to results obtained in previous studies [12, 20, 21, 34].

The results by this study are also compared with calculations done by other researchers in the studies, which demonstrated the strengths of the proposed method. In Fig. 10a, the calculated SWCC for glass beads captures fits much better at lower saturation than the curve simulated by Jaafar and Likos [15] using interpolation of idealized packings, while overestimating the suction a bit in funicular regime. For glass beads in Fig. 10b, the authors did not present any simulation method or results. In Fig.10 c and d, the computed curves in this study approximately fall between the upper bounds and lower bounds by Cao et al. [2], in which ideal packings and circle approximation for meniscus toroid were adopted. The proposed method generally reduced the error in constructions of SWCCs compared to these cited studies.

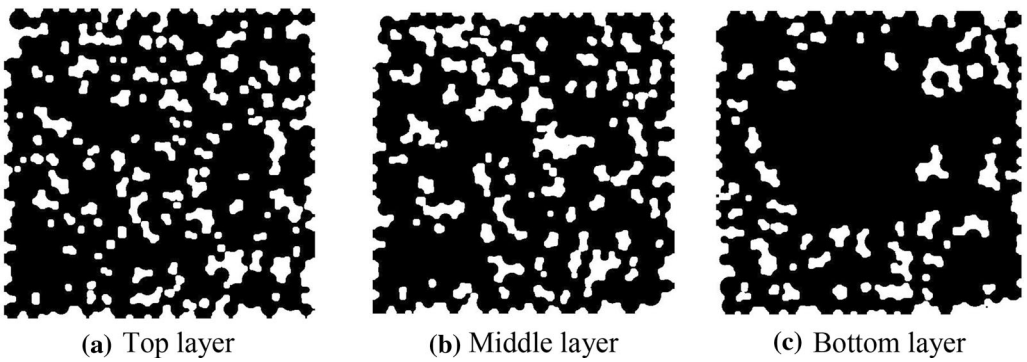

Fig. 9 Horizontal cross sections of the 3D connected pore throats after smoothing, in which the white regions represent the pores and the black regions represent the particles (0.25–0.30 mm glass beads)

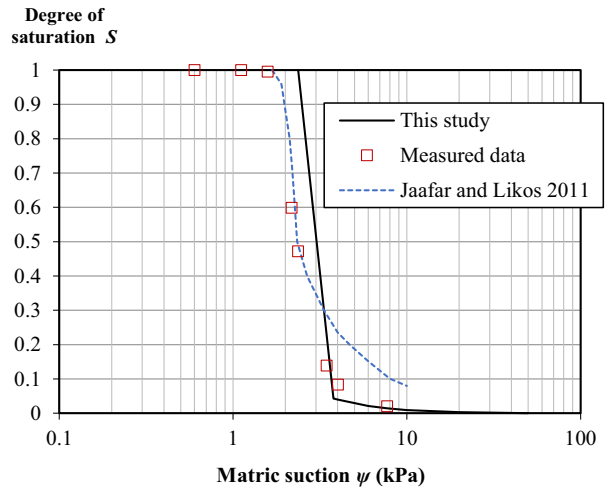

(a) 0.25-0.30 mm glass beads

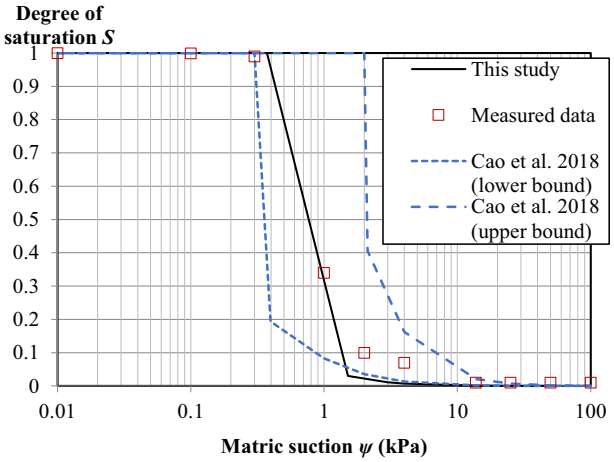

(c) Ottawa 20-20 sand

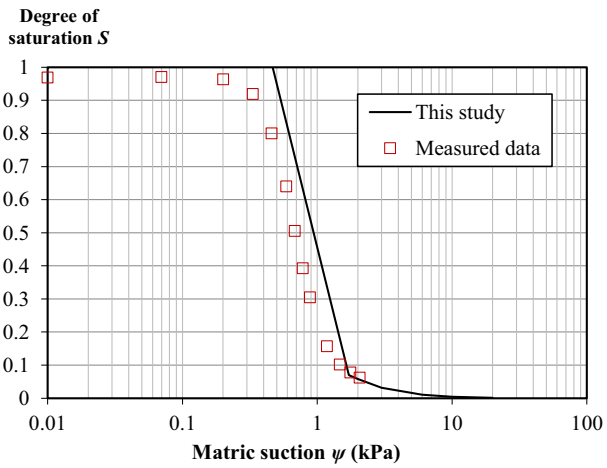

(b) 0.25-0.60 mm glass beads

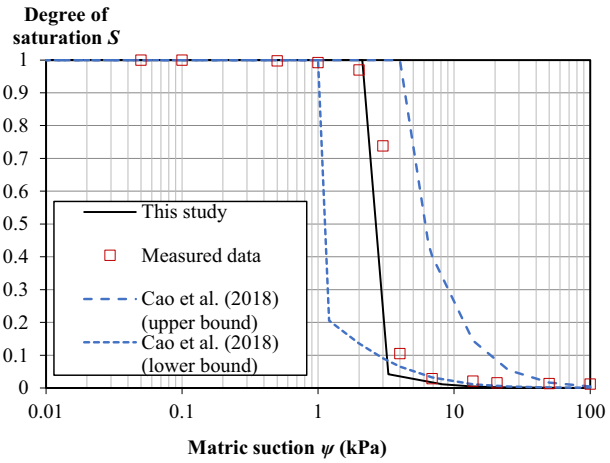

(d) Ottawa 50-70 sand

Fig. 10 SWCCs of Ottawa sands and glass beads, in which the solid lines represent the simulated results and the separated points represent the measured data in literatures

3.5 Modelling of hysteresis of SWCC in drying and wetting processes

Hysteresis phenomenon in drying and wetting is one of the major features of SWCCs for granular materials [16, 22, 37]. There are different hypotheses on the hysteresis behaviours of SWCCs, including the ink-bottle effect, which is dominant in high saturation, and the hysteresis of contact angles in drying and wetting process [20, 21]. The ink bottle is formed in a pore structure with linkage between sections with different diameters. During the drying process, the pore will become desaturate under a higher snap-off suction value, which is controlled by the smaller section at the "bottle neck". During the wetting process, in contrast, the pore will be saturated under a smaller snap-off suction controlled by the larger section at the body of bottle. Besides, contact angles in the wetting process are usually larger than that in the drying process. It is revealed in Fig. 3 that higher contact angle will generate smaller degree of saturation under the same suction for meniscus toroid.

Based on these two mechanisms, the hysteresis of SWCC can be modelled by the following procedures. First of all, modifications can be made on the calculations of funicular regimes presented in Sect. 3.3 to consider the ink-bottle effect. During the wetting process, the snap-off matric suction (ψ_s^i) for the 3D pore throat should be controlled by its minimum value within the whole pore throat (*i.e.* $\psi_s^i = \min\{\psi_s^{i,k}\}, k = 1, 2, \ldots$), instead of the maximum value. Secondly, a larger value of contact angle should be selected for the wetting process, which is usually between 60 and 80 degrees [21]. Following the above two

procedures, the SWCC in the wetting process can be simulated.

Figure 11 shows the results for modelling the hysteresis of SWCC for glass beads 0.25–060 in comparison with the measured data by Manahiloh and Meehan [27]. The contact angle used for the wetting process is 60 degree. In general, the computed curves fit well with measured ones. For the wetting process, the results for the funicular regime seem better, while the computed residual saturation is a bit lower than the measured value. The degree of saturation near AEV is assumed as 100%, which is, however, overestimated. According to the results of experiments by Manahiloh and Meehan [27] and many other researchers, the degree of saturation at AEV is usually smaller than 100% in the wetting process. To properly address this issue, further improvements on the current method are to be conducted.

4 Examination by microscopic photographs and discussions

4.1 Microscopic photographs of water distribution in an unsaturated granular material

To reveal the distribution of water and air in granular materials, a microscopic photography experiment was conducted on unsaturated glass beads. Small glass beads with diameters of 0.4–0.6 mm were fixed inside a transparent acrylic plate frame and immerged in water before testing. Then, the frame was lift above the water level and an unsaturated zone was formed in the glass beads. Due to the capillary effect, the saturation degree inside the material varied with distance from the water level. An industrial camera with magnification lenses was used to take photographs of the glass beads and the water therein.

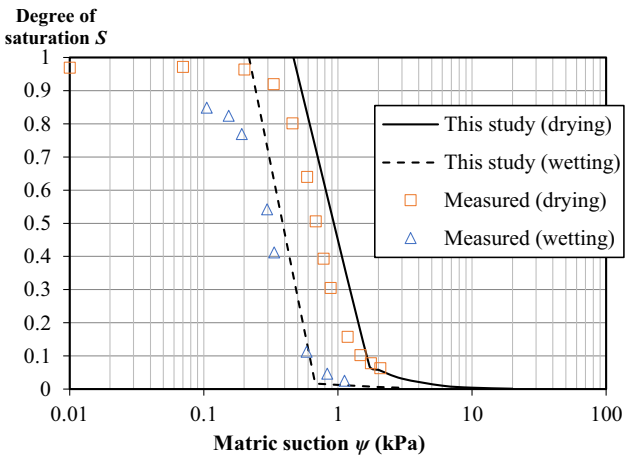

Fig. 11 SWCCs of glass beads 0.25–0.60 in drying and wetting process, in which the lines represent the simulated results and the separated points represent the measured data in studies

Figure 12 shows three microscopic photographs of the glass beads at different heights. Where the saturation degree is low, there exists only meniscus toroid (Fig. 12a). However, a high portion of continuous or patchy water inside the pores can be observed where the degree of saturation is high (Fig. 12b and c). According to the definition in the previous section, Fig. 12a belongs to the pendular regime, while b and c correspond to the funicular regime. The transformation of water phase from the saturated state to the unsaturated state in c and then a was considered as the dominant mechanism of the funicular regime in the calculations in this study.

4.2 Limitations of the proposed method

The proposed method is developed based on the micromechanism of water retention, however, with a series of simplification and assumptions, as revealed in the previous sections. The SWCCs of granular materials predicted with DEM rendition in this study were reasonable for spherical particles (0.25–0.30 mm and 0.25–0.60 mm glass beads), but less reasonable for non-spherical particles (Ottawa 20–30 and 50–70 sands), especially in the pendular regime. There are several reasons contributing to this result, as elaborated in the following paragraphs.

(1) In our method, only capillarity effect is considered in this study. Although meniscus toroid and patchy water are the major forms of fluid in the images in Fig. 12 for glass beads, it is strongly indicated in some previous studies that adsorbed water exists in granular soils [18, 28]. The calculations for adsorbed water have been addressed by different approaches, such as Monte Carlo method in recent studies [25, 38]. Discussions on the effect of adsorption and its dependency on material properties are necessary in further studies to involve the adsorbed water in construction of SWCCs.

(2) In the pendular regime, only meniscus toroid water at the particle contacts was considered in the calculation (Fig. 12a) and all pore throats were assumed unsaturated (i.e. no patchy water). However, patchy water was observed to be possibly the major water component near the residual water content (Fig. 12b), which is discontinuous and cannot be properly simulated by the method in 3.3. In particular, for granular materials with apparent surface roughness or angularity (e.g. Ottawa sand), there will be some smaller pores that cannot be obtained with smooth spheres in the DEM model. According to Eq. (12), smaller pores have higher snap-off suction

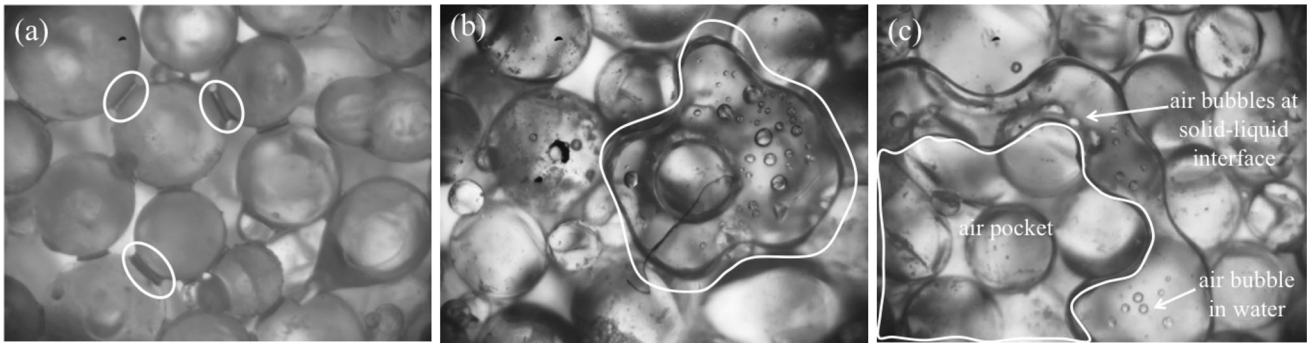

Fig. 12 Microscopic images of **a** toroid water, **b** patchy water, and **c** complicated patterns of air phase, including air pocket, air bubbles in water, and air bubbles in between solid–liquid interfaces

values to lose water and could be still saturated in the pendular regime. Likos and Jaafar [20] studied pore water distribution for F-75 sand and postulated that full pores still play a non-ignorable role in the pendular regime. This could be the major reason why the saturation degree of measured SWCCs was higher than the simulated ones after the residual suction.

(3) High air entry value ceramic disk-based experimental methods (pressure plates, Tempe cell, Fredlund SWCC device) suffer from irreducible saturation at high matric suction due to significantly low hydraulic conductivity in the pendular regime [20], which leads to rather long equilibrium time [10]. Indeed, lacking the flow channel for draining this "isolated" water might be another reason for the high measured degree of saturation in the pendular regime measured by this method.

(4) Spherical particles were adopted in the presented DEM models for simplicity, which are different from the tested Ottawa sand. Such approximation might have changed the contact numbers, pore sizes, and boundary conditions at particle surfaces and result in errors in calculating water content within the particle packings. Therefore, SWCCs for glass beads with regular shapes and smooth surfaces generally perform better compared to those for Ottawa sand.

(5) The method is currently developed for coarse granular materials, assuming that both particle geometry and packing remain unchanged during the drying or wetting process. For other materials, such as bentonite soils [31] with swelling behaviour, the effect of water on the micro-behaviours of particles is more complicated. Adsorbed water and meniscus water at pore throats and inter-particle contacts should be analysed with considerations of the evolutions of particle shape and porosity.

Other possible reasons for the differences between simulated and measured SWCCs include the values of contact angle and other complicated patterns of air phase, such as air pocket, air bubbles in water, and air bubbles in between solid–liquid interfaces (Fig. 12c).

5 Conclusions

The study proposed a new algorithm, which combines microscopic mechanism and discrete element rendition of the real packings of granular materials to simulate their SWCCs. Packing models of four granular materials (glass beads and Ottawa sands) reported previously were reconstructed with Particle Flow Code (PFC). An improved numerical solution to the Young–Laplace equation, which, by adopting an iteration algorithm to directly reveal the generatrix of the meniscus water, was used to calculate the volume of meniscus water between two adjacent spheres. Upscaling of this improved numerical solution by summing up all the volumes of meniscus water between pairs of adjacent spheres in the packing model rendered by PFC yields the SWCC of the pendular regime. To determine the funicular regime of SWCC, an innovative digitized image algorithm is proposed to obtain the information of connected pore throats in the soil sample. By calculating snap-off suction for these pore throats, the upper and lower bounds for the funicular regime of SWCCs can be determined. The proposed method is also extended to model the hysteresis of SWCCs in the drying and wetting process.

The simulated SWCCs agree well with the measured ones in general, especially for the AEVs and residual suctions. SWCCs in the pendular regime for glass beads agree better with the measured ones than those for Ottawa sands. Observation of the water distribution pattern with a microscope reveals that patchy water, instead of toroid water, may be the major form of water for fine-grained granular materials. Not considering the adsorbed water and patchy water in the pendular regime is postulated to be the

most important factor for the difference. Other possible reasons were also mentioned in this study, including limitations of experimental methods, irregular shapes of natural granular materials, contact angle, etc.

Based on the current work, further studies can be conducted to involve patching water, adsorbed water films, irregularly shaped particles in DEM as well as finer irregular particles, such as clayey soils [31]. In addition, shear strength of unsaturated soils is affected by matric suction since the normal stress and cohesion will be influenced by meniscus [39]. Based on the framework of this study, analysis of shear strength for unsaturated soils can be introduced, by quantifying the effect of surface tension at the meniscus of pore throats and inter-particle contacts.

Acknowledgements This research was supported by the Ministry of Science and Technology of China (Award No.: 2019YFC1805002, 2018YFC1802300), the National Natural Science Foundation of China (Award No.: 51779219), and the Basic Science Center Program for Multiphase Evolution in Hypergravity of the National Natural Science Foundation of China (Award No.: 51988101). Financial support from the Overseas Expertise Introduction Center for Discipline Innovation (B18047) is also acknowledged. The financial support to the first author by the One- Thousand-Young-Talents Program of the Organization Department of the CPC Central Committee and the 100-Talents Program of Zhejiang University is deeply appreciated. Supports from a Theme-based Research Scheme project (T22-502/18-R) and a GRF project (PolyU 152209/17E) from Research Grants Council (RGC) of Hong Kong Special Administrative Region Government of China are also acknowleged. The authors would also like to acknowledge the MOE Key Laboratory of Soft Soils and Geoenvironmental Engineering of Zhejiang University and Professor YIN Jian-hua of the Hong Kong Polytechnic University.

Data availability All data, codes, and materials generated or used during the study are available from the corresponding author by request.

Compliance with ethical standards

Conflict of interest The authors declare that they have no competing interest of their own.

References

1. Bittelli M, Flury M (2009) Errors in water retention curves determined with pressure plates. Soil Sci Soc Am J 73(5):1453–1460
2. Cao J, Jung J, Song X, Bate B (2018) On the soil water characteristic curves of poorly graded granular materials in aqueous polymer solutions. Acta Geotech 13(1):103–116
3. Cho GC, Santamarina JC (2001) Unsaturated particulate materials - Particle-level studies. Journal of Geotechnical and Geoenvironmental Engineering 127(1):84–96
4. Fisher RA (1926) On the capillary forces in an ideal soil; correction of formulae given by W. B. Haines. J Agric Sci 16(3):492–505
5. Fredlund DG (2006) Unsaturated soil mechanics in engineering practice. J Geotech Geoenviron Eng 132(3):286–321
6. Fredlund DG, Rahardjo H (1993) Soil mechanics for unsaturated soils. Wiley, Hoboken
7. Fredlund DG, Xing AQ (1994) Equations for the soil-water characteristic curve (VOL 31, PG 521, 1994). Can Geotech J 31(6):1026–1026
8. Fredlund DG, Morgenstern NR, Widger RA (1978) Shear-strength of unsaturated soils. Can Geotech J 15(3):313–321
9. Gan Y, Maggi F, Buscarnera G, Einav I (2013) A particle–water based model for water retention hysteresis. Géotech Lett 3(4):152–161
10. Gee GW, Ward AL, Zhang ZF, Campbell GS, Mathison J (2002) The influence of hydraulic non-equilibrium on pressure plate data. Vadose Zone J 1(1):172–178
11. Gens A (1996) Constitutive modelling: application to compacted soils 3. In: Alonso EE, Delage P (eds) Unsaturated soils. Balkema, Rotterdam, pp 1179–1200
12. Gras JP, Delenne JY, Soulié F, Youssoufi MSE (2011) DEM and experimental analysis of the water retention curve in polydisperse granular media. Powder Technol 208(2):296–300
13. He W, Zhao MH, Chen YG, Wang HH (2010) Theoretical study of microscopical mechanisms and computational method of hysteresis in SWCCs. Rock and Soil Mechanics 31(4):1078–1083
14. Itasca (2016) PFC 5.0 manual, Itasca Consulting Group Inc
15. Jaafar R, Likos WJ (2011) Estimating water retention characteristics of sands from grain size distribution using idealized packing conditions. Geotech Test J 34(5):489–502
16. Kido R, Higo Y, Takamura F, Morishita R, Khaddour G, Salager S (2020) Morphological transitions for pore water and pore air during drying and wetting processes in partially saturated sand. Acta Geotech 15(7):1745–1761
17. Lechman J, Lu N (2008) Capillary force and water retention between two uneven-sized particles. J Eng Mech 134(5):374–384
18. Leverson SM, and Lohnes, RA (1995) Moisture tension relations in sand. Proc, 1st Int Conf. on Unsaturated Soils
19. Lian G, Thornton C, Adams MJ (1993) A theoretical study of the liquid bridge forces between two rigid spherical bodies. J Colloid Interface Sci 161(1):138–147
20. Likos WJ, Jaafar R (2013) Pore-scale model for water retention and fluid partitioning of partially saturated granular soil. J Geotech Geoenviron Eng 139(5):724–737
21. Likos WJ, Lu N (2004) Hysteresis of capillary stress in unsaturated granular soil. J Eng Mech 130(6):646–655
22. Li L, Zhang X, Li P (2019) Evaluating a new method for simultaneous measurement of soil water retention and shrinkage curves. Acta Geotech 14(4):1021–1035
23. Lu N, Kim T, Sture S, Likos WJ (2009) Tensile strength of unsaturated sand. J Eng Mech-ASCE 135(12):1410–1419
24. Lu N, Lechman J, Miller KT (2008) Experimental verification of capillary force and water retention between uneven-sized spheres. J Eng Mech 134(5):385–395
25. Lu N, Zeidman B, Willson C, Lusk M, Wu DT (2010) A Monte Carlo paradigm for capillarity in porous materials. Geophys Res Lett. https://doi.org/10.1029/2010GL045599
26. Lu YF, Chen GF, Luo XQ, Cui YJ (2008) Study of soil-water characteristical curve and its influential factors. Rock Soil Mech 29(9):2481–2486
27. Manahiloh KN, Meehan CL (2015) Evolution of interphase contact angle in partially saturated granular soils using digital analysis of X-Ray computed tomography images. Geotechnical Special Publication (256):2092–2101
28. Mason TG, Levine AJ, Ertas D, Halsey TC (1999) Critical angle of wet sandpiles. Phys Rev E 60(5A):R5044–R5047
29. Mindlin RD, Deresiewicz H (1953) Elastic spheres in contact under varying oblique forces. J Appl Mech 20(3):327–344

30. Mitarai N, Nori F (2006) Wet granular materials. Adv Phys 55(1–2):1–45
31. Ni H, Liu J, Guo J, Yang D, Chen Y (2020) Numerical modelling on water retention and permeability of compacted GMZ bentonite under free-swelling conditions. Int J Numer Anal Meth Geomech 44(12):1619–1633
32. Orr FM, Scriven LE, Rivas AP (1975) Pendular rings between solids: meniscus properties and capillary force. J Fluid Mech 67(4):723–742
33. Sheng D, Zhou A-N (2010) Coupling hydraulic with mechanical models for unsaturated soils. Can Geotech J 48:826–840
34. Suits LD, Sheahan TC, Jaafar R, Likos WJ (2011) Estimating water retention characteristics of sands from grain size distribution using idealized packing conditions. Geotech Test J 34(5):103594
35. van Genuchten MT (1980) A closed-form equation for predicting the hydraulic conductivity of unsaturated soils. Soil Sci Soc Am J 44(5):892–898
36. Wan R, Pouragha M, Eghbalian M, Duriez J, Wong T (2019) A probabilistic approach for computing water retention of particulate systems from statistics of grain size and tessellated pore network. Int J Numer Anal Meth Geomech 43(5):956–973
37. Wen T, Shao L, Xiaoxia Guo X, Zhao Y (2020) Experimental investigations of the soil water retention curve under multiple drying–wetting cycles. Acta Geotech 15(11):3321–3326
38. Zeidman BD, Lu N, Wu DT (2016) Hysteresis of liquid adsorption in porous media by coarse-grained Monte Carlo with direct experimental validation. J Chem Phys 144(17):174709
39. Zhai Q, Rahardjo H, Satyanaga A, Dai G (2019) Estimation of unsaturated shear strength from soil–water characteristic curve. Acta Geotech 14(6):1977–1990
40. Zhang X, Lytton RL (2009) Modified state-surface approach to the study of unsaturated soil behavior part I: basic concept. Can Geotech J 46(5):536–552